Relationship between Boreal Summer Circulation Trend and Destructive Stationary-Transient Wave Interference in the Western Hemisphere

Dong Wan Kim^{1,2} and Sukyoung Lee¹ ¹Department of Meteorology and Atmospheric Science, The Pennsylvania State University, University Park, Pennsylvania ²Corresponding author address: Dong Wan Kim, Department of Meteorology and Atmosp heric Science, Walker Building 407, University Park, PA, 16802 Corresponding author email: dxk582@psu.edu

Abstract

35

36

37

38

39

40

41

42

43

44

45

46

47

48

49

50

51

52

53

54

This study examines the role of the latent heating in exciting the upper-level circulation anomaly which destructively interferes with the climatological stationary wave in the Western Hemisphere during boreal summer. This destructive interference pattern closely resembles the circulation trend which is known to be responsible for surface heat extreme trends. To investigate the mechanism behind this circulation anomaly, daily stationary-transient wave interference and related meteorological variables are analyzed using reanalysis data for the period of 1979-2017. Numerical model simulations forced by reanalysis heating anomalies indicate that the destructive interference pattern is most effectively excited by latent heating anomalies over the North Pacific and eastern Canada. The North Pacific heating anomaly drives circulation anomalies that not only resemble the destructive interference pattern, but also transport moisture into eastern Canada. The resulting latent heating over eastern Canada drives circulation that further reinforces the destructive interference pattern which includes a prominent high pressure system over Greenland. Tropical heating also plays a role in driving the destructive interference pattern. On intraseasonal time scales, the destructive interference pattern is preceded by suppressed Indo-western Pacific heating and enhanced North American monsoon heating. On decadal time scales, both heating centers have strengthened, but the trend of the North American monsoon heating was greater than that of the Indo-Western Pacific heating. These uneven heating trends help explain the resemblance between the destructive interference pattern and the circulation trend over the Western Hemisphere.

55

56

57

58

59

60

1. Introduction

With more frequent occurrence of summer heat waves in recent decades, understanding the mechanism of their excitation has become an important research topic. There is a large body of literature pointing out the importance of the atmospheric circulation in generating surface heat extreme conditions (e.g., Trenberth and Branstator 1992; Lyon and Dole 1995; Lau and Kim 2012; Trenberth and Fasullo 2012; Teng et al. 2013; Wulff et al. 2017). Adding to these earlier results, Lee et al. (2017) have found that the recent trend of boreal summer heat extremes is related to a particular upper level circulation system. They applied a cluster analysis on 200-hPa geopotential field for the period of 1979-2012, and identified a quasi-stationary pattern whose frequency of occurrence had dramatically increased since the late 1990s. This pattern closely resembles the total trend pattern of the upper tropospheric circulation during the examined time period (Baggett and Lee 2019; BL19 hereafter).

Figure 1a shows the linear trend pattern of the 300-hPa streamfunction field during June, July, and August (JJA) for the period of 1979-2017. With midlatitude wavy features whose scale corresponds to zonal wavenumber 5, this trend pattern shares similarities with other previously examined teleconnection patterns, such as the Circumglobal Teleconnection pattern (CGT; Branstator 2002; Wang et al. 2012; Teng et al. 2019), the Silk Road pattern (Enomoto et al. 2003), and the CO₂ forced wave pattern (Baker et al. 2019) over mid-latitudes. However, none of these patterns captures the high pressure anomaly over Greenland shown in Figure 1a. The occurrence of this circulation pattern over Greenland is likely to help account for the recent Greenland warming (Tedesco et al. 2016). This possibility serves as an additional motivation for better understanding the driving mechanism of the circulation trend pattern.

One noteworthy feature of this trend pattern is its striking resemblance to the *opposite* phase of the climatological stationary waves (black contours in Figs. 1a) in the Western Hemisphere (WH). The facts, that latent heating plays the dominant role in driving the summer

stationary wave (Ting 1994) and that there has been an attempt to understand future changes of summer stationary waves from mechanisms involving moist processes (Wills et al. 2019), raise a question as to whether changes in the latent heating field are largely responsible for generating the trend pattern. BL19 also highlighted the importance of latent heating by showing that their idealized diabatic heating over Baffin Bay can generate the upper level high pressure anomaly over Greenland and downstream Eurasian wave trains that resemble the trend pattern. Because the surface turbulent latent heat flux trend over Baffin Bay was downward over the same time period, BL19 concluded that a possible source of the diabatic heating over Baffin Bay is through the release of a latent heat caused by horizontal moisture flux convergence rather than local evaporation. However, the process that initiates the moisture intrusion remains to be examined.

Motivated by the aforementioned studies, we investigate what are the key regions of latent heating that help excite the anomalous circulation that opposes the climatological stationary wave, and what initiates the northward moisture transport into Baffin Bay. Ting (1994) showed that Indo-western Pacific heating drives stationary waves in both the Eastern Hemisphere (EH) and WH, but that heating associated with the North American monsoon region drives a stationary wave over the WH that opposes the stationary wave driven by the Indo-western Pacific heating. This result suggests that changes in the diabatic heating field is likely to be an important driver behind the circulation trend. Specifically, we hypothesize that the North American monsoon heating (WH heating) has been strengthening more than the Indowestern Pacific heating (EH heating), causing the destructive interference pattern to resemble the circulation trend patter in the WH.

The EH tropical heating, however, might still contribute to the WH destructive interference pattern in an indirect fashion. In the context of boreal winter stationary-transient wave interference, Park and Lee (2019) showed that extratropical heating is not independent

of tropical heating; tropical heating anomalies drive circulation anomalies which transports water vapor to the extratropics where some of the water vapor condenses. Therefore, the EH heating could contribute to the WH destructive pattern by transporting moisture into eastern Canada and Baffin Bay where the moisture condenses. The resulting latent heat could then excite the destructive interference pattern. Also, this idea of the remote response to EH tropical heating is in line with earlier findings that the annual circulation trend pattern over the Canadian Arctic and Greenland is forced from the tropical Pacific (Ding et al. 2014), and that the Indian monsoon can influence Arctic ice melting (Krishnamurti et al. 2015)

Data and detailed methodologies are presented in Section 2. In order to test these hypotheses, we first analyze wave activity fluxes (Takaya and Nakamura 2001), latent heating, and moisture fluxes associated with WH destructive interference events using observational data (Section 3). The causalities suggested by these observational data analyses are then tested using initial-value model calculations in Section 4. The conclusions follow in Section 5.

2. Data and Methodology

i. Data

We use daily zonal and meridional wind, 2m-temperature, vertical integral of water vapor flux, and vertical integral of moisture flux divergence from the European Centre for Medium Range Weather Forecasts reanalysis (ERA-Interim; Dee et al. 2011). All variables have a horizontal resolution of 2.5° by 2.5°, and the zonal and meridional wind have 23 vertical pressure levels. Diabatic heating field is obtained from the Japanese 55-year reanalysis (JRA-55; Kobayashi et al. 2015), which has a horizontal resolution of 2.5° by 2.5° and 37 pressure levels. The non-radiative diabatic heating output from the ERA-Interim sums the latent heating and heating due to vertical diffusion, whereas the JRA-55 provides the convective heating, large-scale condensational heating, and vertical diffusive heating separately. As the latent

heating is of our main interest, we opt to use the diabatic heating data from the JRA-55 reanalysis. Overall, there is good agreement between these two reanalysis data sets in both diabatic heating and circulation variables (Park and Lee 2019, and references therein). In this study, following Park and Lee (2019), large-scale condensational heating and convective heating are combined and vertically averaged from 950hPa to 150hPa level, to denote the latent diabatic heating, Q. The time period examined was June, July, and August (JJA) from 1979 to 2017. In this study, anomalies are obtained by first computing a seasonal cycle, which is a smoothed calendar day mean, and then subtracting the seasonal cycle from the raw values. Anomalous diabatic heating and vertical integral of moisture flux divergence field are spatially smoothed by applying two iterations of the "smth9" function of the National Center for Atmospheric Research Command Language (NCL; NCAR Command Language 2016) which uses nine local grid points for the smoothing. The significance levels of the linear trends of variables are computed using the Mann-Kendall test (Wilks 2011).

ii. Stationary Wave Index

We construct the stationary wave index (SWI), which measures the sign and amplitude of the daily interference between transient eddies and the climatological stationary wave (Goss et al. 2016; Park and Lee 2019) by projecting the daily transient eddy streamfunction onto the climatological eddy streamfunction:

$$SWI(t) = \frac{\sum_{i} \sum_{j} \psi'^{*}(\lambda_{i}, \theta_{j}, t) \overline{\psi}^{*}(\lambda_{i}, \theta_{j}, d) \cos(\theta)}{\sum_{i} \sum_{j} [\overline{\psi}^{*}(\lambda_{i}, \theta_{j}, d)]^{2} \cos(\theta)},$$
(1)

where ψ'^* refers to the 300-hPa daily eddy streamfunction anomaly, and $\overline{\psi}^*$ indicates the 300-hPa seasonal cycle eddy streamfunction. Here, eddies are defined as the deviation from the zonal average. The variables λ_i and θ_j refer to the longitude and the latitude at grid point i and j, respectively. The variable t refers to JJA days from 1979 to 2017, and d refers to the

corresponding calendar day.

As indicated in the introduction, the similarity between the circulation trend and the stationary wave occurs mainly over the WH. Therefore, we focus on destructive interference over the WH domain (15°N-75°N, 180°W-0°; green box of Fig. 1b). Destructive interference refers to days when the SWI is less than -1.0. In order to examine the daily evolution of the composite field, we have selected event peaks in the destructive interference, which corresponds to destructive interference days when the SWI values are local minima that are separated from each other by at least 7 days. If another peak with weaker magnitude occurs within that 7-day period, it is discarded. Based on this procedure, 132 destructive interference events are identified, and they are used to composite meteorological variables. Statistical significance of the composite samples is tested by the Monte Carlo resampling method. We generated 1000 random composites, with an equal sample size (132 "events"), to construct a probability distribution.

iii. Trend Index and Heating Projection

We define two additional indices, the trend index (TI) in order to quantify the relationship between the destructive interference and the trend pattern, and the heating projection index (HPI) to evaluate the relationship between latent heating and destructive interference. The TI measures the similarity between daily eddy field and the circulation trend pattern, and is obtained by projecting the daily 300-hPa eddy streamfunction anomaly onto the trend pattern:

$$TI(t) = \frac{\sum_{i} \sum_{j} \psi'^{*}(\lambda_{i}, \theta_{j}, t) \Delta \psi^{*}(\lambda_{i}, \theta_{j}) cos\theta}{\sum_{i} \sum_{j} [\Delta \psi^{*}(\lambda_{i}, \theta_{j})]^{2} cos\theta},$$
(2)

where $\Delta \psi^*$ refers to the linear trend of the JJA seasonal mean 300-hPa eddy streamfunction. Positive TI events are defined to be days when the index in (2) is greater than 1.0 and separated by 7 or more days. The HPI is obtained by projecting the daily heating field onto the climatological heating field:

184
$$HPI(t) = \frac{\sum_{i} \sum_{j} Q'(\lambda_{i}, \theta_{j}, t) \bar{Q}(\lambda_{i}, \theta_{j}, d) \cos \theta}{\sum_{i} \sum_{j} \bar{Q}(\lambda_{i}, \theta_{j}, d)^{2} \cos \theta},$$
(3)

where Q' and \bar{Q} refer to the daily anomalous heating and the seasonal cycle heating, respectively. Positive (negative) heating events are defined as the times when HPI is greater (less) than 1.0 (-1.0). HPI events are defined to be local maxima and minima of the HPI timeseries, separated by at least 7 days. The projection domain for the TI is identical to the SWI index. For the heating projection index, HPI, the EH-heating region (30°S-30°N, 60°E-170°W) and the WH-heating region (30°S-30°N, 120°W-60°W) are projected separately, hence there are two HPIs. These two domains were chosen based on the two centers of tropical heating considered by Ting (1994), indicated in Fig. 3 with the green boxes.

iv. Model setup

In order to examine the hypothesis that destructive interference events are driven by certain latent heating anomalies, we perform model experiments using the spectral dynamical core from Geophysical Fluid Dynamics Laboratory (GFDL). The model set up is identical to that used by Baggett et al. (2016), BL19, and Park and Lee (2019), and is designed to investigate intraseasonal timescale responses to perturbations, such as latent heating, in a specified background state. In our study, the background state is the 1979-2017 JJA climatology of zonal wind, meridional wind, temperature, and surface pressure, which are derived from the monthly mean data of the ERA-interim reanalysis. Because the climatological flow is not a balanced state, in order to ensure that the initial state is a solution to the model equations, a forcing term is added. The forcing term is obtained by integrating the model forward in time one-time step (Franzke et al. 2004). The advantage of this model set up is that it allows one to examine circulation response embedded in a background state of one's choice, but the added

forcing also introduces an inaccuracy whose effect cannot be ignored after about 20 days into the integration (Franzke et al. 2004). Although the dynamic core does not include moist processes, specific humidity is used to initialize the passive tracer field to investigate how moisture is transported by the circulation response. The model has 28 vertical sigma levels and a triangular 42 horizontal resolution. The model uses fourth-order horizontal diffusion with 0.1-day damping time scale at its smallest length scale, with the Held and Suarez (1994) Newtonian cooling and Rayleigh friction parametrizations. The model is forced with time-evolving heating anomaly composites during destructive interference events as in Park and Lee (2019). At model day 1, the model is forced with the lag-day -10 heating composite, at day 2 with the lag-day -9 heating composite, and so on. Therefore, the resulting solution at model day 11 can be compared with lag-day 0 composite. The forcing is applied until model day 17 (lag day +6), and each of the model runs is integrated for 25 days. The heating data, which has 37 pressure levels, was interpolated into the 28 sigma levels prior to making the composite.

3. Observational Data Analyses

i. Structure of the destructive interference pattern

As indicated in the introduction, for the WH, the eddy streamfunction trend opposes the climatological stationary waves (Fig. 1a). Accordingly, composites of the WH destructive interference events, based on negative values of the SWI index, and shown in Fig. 1b, closely resemble the trend pattern in the WH. We further quantified this similarity by compositing the stationary wave index (SWI) for positive TI events, as well as composites of the TI index for destructive SWI events. Figure 1c shows that, at lag day 0 for positive TI events, the SWI is -0.73 (blue line). Conversely, the lag day 0 composite TI index for destructive SWI events is 0.75 (red line). The magnitudes of these values are not much smaller than the threshold value of the positive (destructive) TI (SWI) events, which is 1.0 (-1.0). This solid relationship

indicates that more frequent and/or stronger destructive interference events likely make an important contribution to the WH circulation trend, and motivates us to investigate the dynamical processes that cause the destructive interference. The same analysis for the EH reveals no statistically significant values (not shown), confirming the visual impression from Fig. 1a that the EH trend pattern is unrelated to changes in stationary wave amplitude.

The time evolution of the 300-hPa eddy streamfunction anomaly composites, based on negative values of the SWI, indicates that destructive interference events take place over a time period of about ten days (Fig. 2a-c). The initial development of the northeastern Pacific anticyclone coincides with a poleward and eastward wave activity flux over the central North Pacific, while that of the Greenland anticyclone appears to be associated with a wave activity flux emanating from North America (Fig. 2a). Within the next five days, the major features of the destructive interference pattern are established, with the anticyclones over the northeastern Pacific and Greenland, and the cyclones over North America and the North Atlantic (Fig. 2b). At these lags, the wave activity flux propagates from the northeastern Pacific to Greenland. These circulation and wave activity flux signals weaken over the next five days (Fig. 2c). These results suggest that the primary wave activity source for the WH destructive interference is located over the extratropical North Pacific. This possibility is examined in section 3iii.

A comparison between the composite streamfunction fields, based on destructive SWI events, with the corresponding 2-m temperature composite fields indicates that the temperature anomalies (Fig. 2d-f), associated with the WH destructive interference events, in general, coincide with the upper level circulation pattern. The high pressure regions of Greenland and eastern Canada experience positive temperature anomalies while the low pressure regions of North America and the North Atlantic show negative anomalies (Fig. 2e). Over the oceans, including Baffin Bay, the 2-m temperature anomalies associated with the upper level circulation are much weaker. Because it takes much longer for the ocean temperature to respond

to heating due to its higher heat capacity, this difference in the temperature anomaly amplitude between the land and the ocean suggests that the surface temperature anomalies mostly reflect a response to the atmospheric circulation aloft.

ii. Role of the tropical heating

First, we test the hypothesis discussed in section 1 that the WH destructive interference is associated with amplified WH climatological tropical heating and muted EH climatological tropical heating. As was hypothesized, the two centers of tropical heating exhibit opposite signs in their anomalies. That is, a calculation of the composite diabatic heating anomalies based on destructive events of the SWI finds that negative heating anomalies prevail for the region of the EH heating (30°S-30°N, 60°E-170°W; left green boxes of Fig. 3), while the WH heating anomalies are weakly positive (30°S-30°N, 120°W-60°W; right green boxes of Fig. 3). Similar features are also captured with composites of the two HPIs (Fig. 4a) for the destructive interference events. As can be seen, the EH-heating projects negatively onto the EH climatological heating, especially during earlier lag days. On the other hand, the WH-heating projects positively onto the WH climatological heating centered at lag days -7 and 0, although the amplitude weakens in between these two peaks. This result indicates that when destructive interference occurs in the WH, the EH-heating (WH-heating) structure is opposite from (similar to) that of the climatological heating. These opposite signals of two heating centers are in line with the stationary wave theory of Ting (1994).

Next, we address the hypothesis that the upward trend in the destructive interference pattern is accompanied by a strengthening of the WH tropical heating, and/or a weakening or muffled strengthening of the EH tropical heating. We show in Fig. 4b the frequency timeseries of positive WH and EH heating events. Each value of timeseries represents the number of positive events in a given year. For both the EH heating and the WH heating, the frequency of

positive events has been trending upward over the period of 1979 to 2017, indicating that the climatological heating in the tropics has been intensifying. However, the trend in the frequency of the WH-heating events is greater than that of the EH-heating events. The slope of the linear fit of the WH-heating event frequency is 0.097 events/year, which is greater than that of the EH-heating event frequency, which is 0.071 events/year. We regressed JJA mean 300-hPa eddy streamfunction onto timeseries of positive events of two heating projections and found that the magnitudes of the two regressed streamfunction fields are comparable (not shown). Based on this result, we conclude that the trend in the WH heating frequency being larger than the EH heating frequency trend has contributed to the similarity between WH destructive interference pattern and the circulation trend during the analysis period.

iii. Midlatitude heating and heating-circulation relay mechanism

The wave activity flux that we examined in Section 3i indicates that there is a source of wave activity in the northeastern corner of the North Pacific, suggesting that midlatitude forcing also plays an important role in driving the destructive interference pattern. Consistent with this interpretation, prior to the full development of the destructive interference events, there is a positive latent heating anomaly in the same region (Fig. 3a; blue box). This heating anomaly pattern agrees with horizontal moisture flux convergence pattern a day earlier (Fig. 3d), suggesting that the North Pacific latent heating arises from condensation of moisture transported from elsewhere. Composites of the water vapor flux vectors shows that these vectors extend to the subtropical western Pacific (Fig. 3d). As the North Pacific heating and moisture flux convergence diminish over the next five days (Figs. 3b,e), a positive heating anomaly starts to develop over eastern Canada (Fig. 3b; red box): During the lag day –4 to 0 interval, a cluster of water vapor flux vectors emerge over the North Atlantic and eastern North America that enters eastern Canada (Fig. 3e).

The water vapor flux vectors in Fig. 3e indicate that the moisture itself originates from the North Atlantic, but the wave activity flux vectors shown in Fig. 2 indicate that the circulation anomalies that cause the moisture fluxes are driven by the wave activity source over the North Pacific. These moisture fluxes converge over eastern Canada (Fig. 3e), consistent with the latent heating release also over eastern Canada (Fig. 3b). The eastern Canada heating anomaly and moisture flux convergence start to dissipate after lag day +1 (Figs. 3c,f). BL19 mimicked this eastern Canada heating anomaly with an idealized heating structure, and found that the heating can generate a wave train with a high pressure over Greenland that resembles the observed Greenland high. These results paint a picture of a heating-circulation relay mechanism similar to the one described in Park and Lee (2019). Specifically, subtropical western Pacific heating anomaly excites circulation anomalies which transport moisture from southwest of the region denoted by the blue box in Fig. 3a into the northeastern corner of the North Pacific, and the resulting moisture flux convergence and latent heating drives a circulation pattern that destructively interferes with the climatological stationary wave; the resulting circulation pattern then transports moisture from North Atlantic to North America and then to eastern Canada, where again there is moisture flux convergence and condensation, leading to the excitation of the Greenland circulation anomaly farther downstream.

303

304

305

306

307

308

309

310

311

312

313

314

315

316

317

318

319

320

321

322

323

324

325

326

327

The lead-lag relationship between the North Pacific and eastern Canada heating anomalies is quantified by constructing daily time series of the two heating anomalies for these two domains. Figure 5 shows composites of the normalized daily heating anomalies, averaged (area-weighted) over the North Pacific domain (40°-70°N/170°-140°W; blue boxes in Figs. 3a,d) and the eastern Canada domain (40°-70°N/90°-60°W; red boxes in Figs. 3b,e), for the destructive interference events. These normalized anomaly time series are referred to as the North Pacific and the eastern Canada heating indices, respectively. The North Pacific heating index peaks at lag day –6 and the peak of the eastern Canada heating index follows at lag day

-1, with the amplitudes of these peaks both being statistically significant. The suggested causal relationship between these two heating centers is tested in the section 4 with model experiments.

4. Model Experiments

328

329

330

331

332

333

334

335

336

337

338

339

340

341

342

343

344

345

346

347

348

349

350

351

352

In this section, we explore the ideas that arose from the observational analyses by examining the circulation responses to observed heating anomalies. We specifically ask two questions. First, does the North Pacific heating generate the destructive interference pattern over the WH? Second, does the North Pacific heating excite circulation anomalies that transport moisture into eastern Canada? In order to address these questions in a systematic fashion, we conduct a set of experiments by forcing the model with a series of patch forcings, which have a size of 30° latitude by 30° longitude. The heating for each patch corresponds to the composite heating of the destructive interference events for the domain of that patch. The center of each square patch ranges from 15°S to 75°N, and from 5°E to 5°W, with a 10° increment in both the latitudinal and longitudinal directions. For example, the first (last) model run is forced with the observed heating composite, over the domain of 30°S to 0° and 10°W to 20°E (60°N to 90°N and 20°W to 10°E), with zero heating elsewhere. This experiment yields a total of 360 model simulations. Next, in order to evaluate how similar each of these simulated circulation fields is to the observed pattern of destructive interference, we computed uncentered pattern correlations between model streamfunction responses and the observed streamfunction composite, both at the 300-hPa level, for the extratropical WH domain, i.e., from 30°N to 90°N, and from 180°W to 0°. In order to reduce day-to-day noise in these flow fields, prior to computing the pattern correlations, the observed composite fields are averaged from lag days -5 to +5, and the model responses are averaged over model days 6 to 16. As the model at day 1 is forced by the heating composite at lag day -10, model days 6 to 16 correspond to observational lag days -5 to +5. There are 360 pattern correlation values corresponding to the 360 forcing patches. The 360 pattern correlation values are presented with a map which is

shown in Fig. 6. At each location, the values in Fig. 6 correspond to the pattern correlation for the patch forcing centered over that location. Specifically, the pattern correlation value that results from each patch forcing is assigned to the center of the patch domain. Accordingly, Fig. 6 shows the domain covered by the patch centers which range from 15°S to 75°N, and 5°E to 5°W. For a given location, the red (blue) shading indicates that the model circulation response to the composite patch heating at that location matches (opposes) the observed circulation over the pattern correlation domain.

i. Circulation response

353

354

355

356

357

358

359

360

361

362

363

364

365

366

367

368

369

370

371

372

373

374

375

376

From the model experiments described above, we identify two prominent forcing regions: the North Pacific and eastern Canada (Fig. 6). The positive pattern correlations over these regions indicate that the heating anomalies centered at these two regions drive circulation responses most similar to the destructive interference composite in the WH extratropics. The model eddy streamfunction responses are shown with shading in the left column of Fig. 8, where for ease of comparison the destructive interference composite of eddy streamfunction anomalies are indicated with contours. Within the North Pacific forcing domain, the heating over the 20°-50°N/180°-150°W domain generates circulation anomalies that best match with the destructive interference composite, having a pattern correlation of 0.57 (Fig. 8a). This forcing patch generates high pressure over the northeastern North Pacific and the eastern Canada regions and low pressure over North America and the North Atlantic. Another important forcing location is the eastern Canada region. The 40°-70°N/90°-60°W patch forcing, with a pattern correlation of 0.65, drives a wave train over Greenland and the North Atlantic that resembles the overlaid destructive inference anomaly field (Fig. 8b). This circulation response resembles the result of BL19. If the model is forced by these two patch domains simultaneously, the pattern correlation increases to 0.78 (Fig. 8c).

In addition to these two regions, tropical heating also produces a positive pattern correlation, albeit with weaker magnitude. The WH tropical heating generates circulation anomalies similar to that of the destructive interference pattern, as indicated by the positive pattern correlation over Central America in Fig. 6. This map also indicates that the EH tropical heating anomalies yield mixed results, with the heating anomalies over the Indian monsoon and western Pacific warm pool contributing to the destructive interference pattern, while the heating anomaly centered at around 100°E damps the destructive interference pattern.

ii. Passive tracer response

377

378

379

380

381

382

383

384

385

386

387

388

389

390

391

392

393

394

395

396

397

398

399

400

The model results thus far indicate that latent heating anomalies over the North Pacific and eastern Canada are most effective at generating the destructive interference circulation pattern. Given the evidence of moisture transport into these regions (Fig. 3), we ask which forcing region is most effective at exciting circulation anomalies that can transport moisture into those two regions. We address this question by examining the response of a passive tracer which is initialized with the climatological specific humidity spatial profile. First, in order to identify the patch domain that can most effectively advect a tracer into eastern Canada, vertically integrated tracer anomalies of each model simulation are averaged (area-weighted) over the 40°-70°N/90°-60°W domain, from model day 9 to 11. We chose this particular domain because the model solution, forced with heating in this domain, shows the best match with the destructive interference pattern. Model days 9 to 11 are chosen because they correspond to lag day -2 to 0, when the observed eastern Canada heating peaks (Fig. 5). Using this approach, locations with positive (negative) values in Fig. 7a correspond to locations where the heating field excites circulation anomalies that increase (decrease) the anomalous tracer value over the eastern Canada region. This procedure yields 360 eastern Canada anomalous tracer values, which are shown in Fig. 7a.

Figure 7a reveals that the circulation driven by the North Pacific heating can remotely transport moisture into the eastern Canada domain (red box of Fig. 7a). Specifically, over the North Pacific region, the forcing domain of 40°-70°N/170°-140°W produces the strongest tracer anomalies over the eastern Canada region, with an area-averaged value of 0.14 kg m⁻² (Fig. 7a). The vertical integral of the tracer flux vectors in Fig. 8h suggest that the anomalous southerly flow over eastern North America is responsible for the moisture intrusion into eastern Canada. This southerly flow is part of the cyclonic and anticyclonic circulation pair over central North America and the North Atlantic (Fig. 8d). The pattern correlation resulting for the 40°-70°N/170°-140°W domain forcing is 0.25, which is smaller than that of 20°-50°N/180°-150°W domain. The former domain, however, produces a greater tracer anomaly response over the eastern Canada region (compare the shading Figs. 8e and Fig. 8h). These model results underscore the important role that the North Pacific heating remotely plays for both inducing the WH destructive pattern and the eastern Canada tracer anomaly.

The eastern Canada heating (40°-70°N/90°-60°W) induces a dipole structure of tracer response with positive anomalies over Baffin Bay and negative anomalies over Hudson Bay (Fig. 8f). Again, this model solution closely resembles that shown in BL19 (see their Fig. 7). The tracer response to the combination of the North Pacific and the eastern Canada forcing is shown in Fig. 8g. We used the patch domain of 40°-70°N/170°-140°W to represent the North Pacific forcing for Fig. 8g as this domain gives the best tracer response, whereas we used patch domain of 20°-50°N/180°-150°W for Fig. 8c as it gives best circulation response. Over the eastern Canada region, the tracer structure is similar to that induced by eastern Canada heating alone (Fig. 8f). This result suggests that remote forcing from the North Pacific initiates the moisture intrusion over eastern Canada, and latent heating over eastern Canada drives an even stronger moisture intrusion. Central Canada forcing also gives a strong response to the eastern Canada tracer anomaly (Fig. 7a). However, unlike the North Pacific forcing, patches over

central Canada either locate right next to or even overlap with the eastern Canada patch (red square of Fig. 7a). Therefore, this response is likely a local feedback, whereas the North Pacific patches act on a remote distance.

In a similar manner, we investigate which forcing is most effective at transporting moisture into the North Pacific region. The model tracer responses are averaged over the 40°-70°N/170°-140°W domain during model days 4-6, which corresponds to lag day -7 to -5 when the North Pacific heating anomaly peaks (Fig. 5). This domain is chosen because it is the most important forcing region for generating the eastern Canada tracer anomalies. The result is shown in Figure 7b. The greatest positive tracer anomalies in the North Pacific region are obtained when model is forced by western Pacific heating, centered between 150°E and 180°E, 20°N and 50°N. In accordance with the moisture flux composite (Fig. 3d), this result points out the role of subtropical western Pacific heating in inducing circulation anomalies which advect moisture into the midlatitude North Pacific domain.

5. Conclusions and Discussion

In this study, we have investigated the role of latent heating anomalies in exciting the anomalous circulation pattern that destructively interferes with the climatological stationary wave. This destructive interference pattern, which occurs over the WH, closely resembles the circulation trend pattern that includes the Greenland high. By studying the driving mechanism of the destructive interference pattern, therefore, we can also better understand the mechanism by which the circulation trend pattern arises.

Our analysis reveals two noteworthy findings regarding the role of tropical heating on the destructive interference pattern. First, consistent with stationary wave theory (Ting, 1994), the destructive interference pattern is associated with the suppressed EH tropical heating and the enhanced WH tropical heating. Second, while the climatological heating field has intensified in both hemispheres, the trend of the WH heating is greater than that of the EH heating. Accordingly, the destructive interference pattern has been able to dominate the circulation trend.

450

451

452

453

454

455

456

457

458

459

460

461

462

463

464

465

466

467

468

469

470

471

472

473

474

The WH destructive interference pattern, however, is most effectively excited by latent heating anomalies over the North Pacific and eastern Canada. The schematic diagram shown in Fig. 9 describes how the North Pacific and eastern Canada heating anomalies excite the destructive interference pattern. First, the moisture is transported from the subtropical western Pacific into the northeastern corner of the North Pacific, where that moisture fluxes converge and release latent heating anomalies (Fig. 9a). Those latent heating anomalies over the North Pacific excite the upper level destructive interference pattern (Fig. 9b). Then, another moisture intrusion occurs due to the induced destructive interference pattern, from the Atlantic to eastern Canada where latent heating anomalies are again released (Fig. 9c). Heating anomalies over eastern Canada further excite circulation anomalies to amplify the destructive interference pattern (Fig. 9d). Our finding, that extratropical heating anomalies play the major role, might appear at odds with the prior results which highlighted the role of the tropical heating in warming the Canadian Arctic and Greenland (Ding et al. 2014) and the role of the Indian monsoon on Canadian Arctic ice melting (Krishnamurti et al. 2015). However, the heatingcirculation relay picture of Park and Lee (2019) helps reconcile this apparent difference, because even in our analysis, at least part of the extratropical heating is driven by the circulation excited by the tropical/subtropical heating.

We have examined if transient eddy fluxes contribute to the destructive interference pattern. Specifically, we computed the streamfunction tendency due to high-frequency eddy vorticity flux, which has been examined in previous studies (e.g. Cai and van den Dool 1994; Feldstein 1998; Teng et al. 2019). We found that transient eddy vorticity flux helps to establish the anticyclonic circulation over Greenland, but it does not contribute to the anticyclone over

the North Pacific and cyclones over the North America and the Atlantic (not shown). Therefore, transient eddy fluxes play a contributing role but only limited to Greenland region, and the primary driver of the hemispheric destructive interference pattern is the latent heating anomaly.

One commonly discussed mechanism for the circulation-extreme weather linkage is a 'quasi-resonant amplification' which attributes the extreme weather to amplified atmospheric waves of zonal wave number 6 to 8 (Petoukhov et al. 2013; Mann et al. 2017). However, we find that in the WH the circulation trend actually corresponds to destructive interference, rather than constructive interference. Because the proposed resonant response is circumglobal, we conclude that the coincidence of the destructive interference circulation pattern with the trend pattern is an indication that the quasi-resonant amplification is an unlikely explanation of the circulation and temperature trends in recent decades. Furthermore, the prior finding that there is no statistically significant observed trend of resonance (Screen and Simmonds, 2013; Petoukhov et al. 2013) also supports the idea that the observed circulation trend pattern is unrelated to the resonance mechanism. At least for the WH, our result instead indicates that anomalous latent heating is an important contributor to the trend pattern, which is in line with the studies that show the importance of diabatic forcing in driving anomalous summer circulation (Teng et al. 2019; Baker et al. 2019).

Acknowledgements

We thank Steven Feldstein, Mingyu Park, and Joseph Clark for their discussion on this study. This study was supported by National Science Foundation grants OPP-1723832, AGS-1822015 and AGS-1948667.

References

523

Baggett, C., S. Lee, and S. B. Feldstein, 2016: An investigation of the presence of atmospheric 524 rivers over the North Pacific during planetary-scale wave life cycles and their role in 525 Arctic warming. J. Atmos. Sci., 73, 4329-4347, https://doi.org/10.1175/JAS-D-16-526 0033.1. 527 -., and S. Lee, 2019: Summertime midlatitude weather and climate extremes induced by 528 moisture intrusions to the west of Greenland. Quart. J. Royal Meteor. Soc, 145, 3148-529 3160. https://doi.org/10.1002/qj.3610. 530 Baker, H. S., T. Woollings, C. Mbengue, M.R. Allen, C.H. O'Reilly, H. Shiogama, and S. 531 Sparrow, 2019: Forced summer stationary waves: the opposing effects of direct 532 533 radiative forcing and sea surface warming. Climate Dyn, 53, 4291-4309, https://doi.org/10.1007/s00382-019-04786-1. 534 Branstator, G, 2002: Circumglobal teleconnections, the jet stream waveguide, and the North 535 Atlantic Oscillation. J. Climate, 15, 1893-1910, https://doi.org/10.1175/1520-536 0442(2002)015<1893:CTTJSW>2.0.CO;2. 537 Cai, M., and H. M. van den Dool, 1994: Dynamical decomposition of low-538 frequency tendencies, J. Atmos. Sci., 51, 2086-2100, https://doi.org/10.1175/1520-539 0469(1994)051<2086:DDOLFT>2.0.CO;2. 540 541 Dee, D. P., and Coauthors, 2011: The ERA-Interim reanalysis: configuration and performance of the data assimilation system. Quart. J. Roy. Meteor. Soc., 137, 553-597, 542 https://doi.org/10.1002/qj.828. 543 Ding, Q., J. M. Wallace, D. S. Battisti, E. J. Steig, A. J. Gallant, H. J. Kim, and L. Geng 2014: 544 Tropical forcing of the recent rapid Arctic warming in northeastern Canada and 545 Greenland. *Nature*, **509**, 209-212, https://doi.org/10.1038/nature13260. 546

- Enomoto, T., B. J. Hoskins, and Y. Matsuda, 2003: The formation mechanism of the Bonin high
- 548 in August. *Quart. J. Roy. Meteor. Soc.*, **129**, 157-178,
- 549 https://doi.org/10.1256/qj.01.211.
- 550 Franzke, C., Lee, S., & Feldstein, S. B. (2004). Is the North Atlantic Oscillation a breaking
- 551 wave? J. Atmos. Sci., 61, 145-160, https://doi.org/10.1175/1520-
- 552 0469(2004)061<0145:ITNAOA>2.0.CO;2.
- Feldstein. S., 1998: The growth and decay of low-frequency anomalies in a GCM. J. Atmos.
- 554 Sci., 55, 415-428, https://doi.org/10.1175/1520-
- 555 0469(1998)055<0415:TGADOL>2.0.CO;2.
- Goss, M., S. B. Feldstein, and S. Lee, 2016: Stationary wave interference and its relation to
- tropical convection and Arctic warming, J. Climate, 29, 1369–1389,
- 558 https://doi.org/10.1175/JCLI-D-15-0267.1.
- Held, I. M., and M. J. Suarez, 1994: A proposal for the intercomparison of the dynamical cores
- of atmospheric general circulation models. *Bull. Amer. Meteor. Soc.*, **75**, 1825–1830,
- 561 https://doi.org/10.1175/1520-0477(1994)075<1825:APFTIO>2.0.CO;2.
- Kobayashi, S., and Coauthors, 2015: The JRA-55 reanalysis: General specifications and basic
- 563 characteristics. *J. Meteor. Soc. Japan*, **93**, 5-48, https://doi.org/10.2151/jmsj.2015-001.
- Krishnamurti, T. N., R. Krishnamurti, S. Das, V. Kumar, A. Jayakumar, and A. Simon, 2015: A
- pathway connecting the monsoonal heating to the rapid Arctic ice melt. J. Atmos. Sci.,
- **72**, 5-34, https://doi.org/10.1175/JAS-D-14-0004.1.
- Lau, W. K., and K. M. Kim, 2012: The 2010 Pakistan flood and Russian heat wave:
- Teleconnection of hydrometeorological extremes. J. Hydrometeor., 13, 392-403,
- 569 https://doi.org/10.1175/JHM-D-11-016.1.
- Lee, M. H., S. Lee, H. J. Song, and C. H. Ho, 2017: The recent increase in the occurrence of a

- boreal summer teleconnection and its relationship with temperature extremes. J.
- 572 *Climate*, **30**, 7493-7504, https://doi.org/10.1175/JCLI-D-16-0094.1.
- Lyon, B., and R. M. Dole, 1995: A diagnostic comparison of the 1980 and 1988 US summer
- heat wave-droughts. *J. climate*, **8**, 1658-1675, https://doi.org/10.1175/1520-
- 575 0442(1995)008<1658:ADCOTA>2.0.CO;2.
- Mann, M. E., S. Rahmstorf, K. Kornhuber, B. A. Steinman, S. K. Miller, and D. Coumou, 2017:
- Influence of anthropogenic climate change on planetary wave resonance and extreme
- weather events. *Sci. Rep.*, 7, 45242, https://doi.org/10.1038/srep45242.
- 579 NCAR Command Language, 2019: NCL Version 6. 6. 2. Accessed 7 June 2020,
- 580 http://dx.doi.org/10.5065/D6WD3XH5.
- Park, M., and S. Lee, 2019: Relationship between Tropical and Extratropical Diabatic Heating
- and Their Impact on Stationary–Transient Wave Interference. J. Atmos. Sci., 76, 2617-
- 583 2633, https://doi.org/10.1175/JAS-D-18-0371.1.
- Petoukhov, V., S. Rahmstorf, S. Petri, and H. J. Schellnhuber, 2013: Quasiresonant
- amplification of planetary waves and recent Northern Hemisphere weather extremes.
- 586 *Proc. Nat. Acad. Sci. USA*, **110**, 5336-5341, https://doi.org/10.1073/pnas.1222000110.
- Petoukhov, V., S. Rahmstorf, S. Petri, and H. J. Schellnhuber, 2013: Reply to Screen and
- Simmonds: From means to mechanisms. Proc. Nat. Acad. Sci. USA, 110, E2328,
- 589 https://doi.org/10.1073/pnas.1305595110.
- Screen, J. A., and I. Simmonds, 2013: Caution needed when linking weather extremes to
- amplified planetary waves. Proc. Nat. Acad. Sci. USA, 110, E2327,
- 592 https://doi.org/10.1073/pnas.1304867110.
- Takaya, K., H. Nakamura, 2001: A formulation of a phase-independent wave-activity flux for

stationary and migratory quasigeostrophic eddies on a zonally varying basic flow. J. 594 Atmos. 608-627, https://doi.org/10.1175/1520-595 Sci., **58**, 0469(2001)058<0608:AFOAPI>2.0.CO;2. 596 Tedesco, M., T. Mote, X. Fettweis, E. Hanna, J. Jeyaratnam, J. F. Booth, R. Datta, and K. Briggs, 597 2016: Arctic cut-off high drives the poleward shift of a new Greenland melting record. 598 599 *Nat. Commun.*, 7, 11723, https://doi.org/10.1038/ncomms11723. Teng, H., G. Branstator, A. B. Tawfik, and P. Callaghan, 2019: Circumglobal response to 600 prescribed soil moisture over North America. J. Climate, 32, 4525-4545, 601 https://doi.org/10.1175/JCLI-D-18-0823.1. 602 —., G. Branstator, H. Wang, G. A. Meehl, and W. M. Washington, 2013: Probability of US 603 604 heat waves affected by a subseasonal planetary wave pattern. Nat. Geosci., 6, 1056-1061, https://doi.org/10.1038/ngeo1988. 605 Ting, M., 1994: Maintenance of northern summer stationary waves in a GCM. J. Atmos. Sci., 606 3286-3308, https://doi.org/10.1175/1520-607 51, 0469(1994)051<3286:MONSSW>2.0.CO;2. 608 Trenberth, K. E., and G. W. Branstator, 1992: Issues in establishing causes of the 1988 drought 609 over North America. J. Climate, 5, 159-172, https://doi.org/10.1175/1520-610 0442(1992)005<0159:IIECOT>2.0.CO;2. 611 —, and J. T. Fasullo, 2012: Climate extremes and climate change: The Russian heat wave 612 and other climate extremes of 2010. J. of Geophys. Res., 117, D17103, 613 https://doi.org/10.1029/2012JD018020. 614 Wang, H., B. Wang, F. Huang, Q. Ding, and J. Y. Lee, 2012: Interdecadal change of the boreal 615 summer circumglobal teleconnection (1958–2010). Geophys. Res. Lett., 39, L12704, 616

617	https://doi.org/10.1029/2012GL052371.
618	Wills, R. C., R. H. White, and X. J. Levine, 2019: Northern Hemisphere stationary waves in a
619	changing climate. Curr. Climate Change Rep., 5, 372-389
620	https://doi.org/10.1007/s40641-019-00147-6.
621	Wilks, D. S., 2011: Statistical Methods in the Atmospheric Sciences. 3rd ed. International
622	Geophysics Series, Vol. 100, Academic press. 704 pp.
623	Wulff, C. O., R. J. Greatbatch, D. I. Domeisen, G. Gollan, and F. Hansen, 2017: Tropica
624	forcing of the Summer East Atlantic pattern. Geophys. Res. Lett. 44, 11-166
625	https://doi.org/10.1002/2017GL075493.
626	
627	
628	
629	
630	
631	
632	
633	
634	
635	
636	
637	

Figure Captions

Figure 1. (a) The linear trend of June, July, and August 300-hPa eddy streamfunction during 1979-2017 (shading) and the 300-hPa climatological stationary wave (contour). Contour interval is 2.5×10^6 m² s⁻¹; negative values are dashed and zero value is omitted. (b) 300-hPa eddy streamfunction anomaly composite for destructive stationary wave interference (SWI) index at lag day 0 (shading). The contours are as in (a). Green box indicates the projection domain of SWI. (c) Lagged composite of SWI against positive events of trend index (TI; blue line), and lagged composite of TI against SWI destructive events (red line). Dotted areas in (a) indicate statistical significance at the 95% level as computed by the Mann-Kendall test, and dotted areas in (b) and thick line in (c) indicate statistically significant values at the 95% level as computed by Monte Carlo resampling method.

Figure 2. Pentad composites of (a)-(c) 300-hPa eddy streamfunction anomaly (shading) with wave activity flux (vectors) and (d)-(f) 2m-temperature anomaly. Vectors with magnitude larger than 0.1 m² s⁻² are plotted and the reference vector is 2 m² s⁻². Pentads are centered at lag days –5, 0, and +5 of destructive stationary wave interference (SWI) events. Dotted areas represent statistical significance at the 95% level as computed by the Monte Carlo resampling method.

Figure 3. (a)-(c) Pentad composites of latent diabatic heating anomaly (shading) and June, July, and August (JJA) climatological heating (contour; 2, 4, and 6 K/day values are plotted). (d)-(f) Pentad composites of vertically integrated water vapor flux anomaly (vectors) with vertically integrated moisture flux convergence anomaly (shading). Vectors with magnitude larger than 20 kg m⁻¹ s⁻¹ are plotted and the reference vector is 50 kg m⁻¹ s⁻¹. Pentads are centered at lag days (a)-(c) –6, -1, and +4, and (d)-(f) -7, -2, and +3 of destructive stationary wave interference (SWI) events. Dotted areas represent statistical significance at the 95% level

as computed by the Monte Carlo resampling method. Green boxes represent two domains of tropical heating projection index (HPI) and blue and red boxes represent the North Pacific domain and the eastern Canada domain (see section 3 for details).

Figure 4. (a) Lagged composite of normalized heating projection amplitudes of (blue) the EH-heating and (red) the WH-heating during destructive stationary wave interference (SWI) events. Dots with thick lines indicate statistically significant values at the 95% level as computed by the Monte Carlo resampling method. (b) Timeseries of the number of positive heating projection events per each year. The blue and the red line indicate the heating projection over EH-heating domain and the WH-heating domain, respectively. Dashed lines indicate linear fit lines of each timeseries. Indicated p-values are computed by the Mann-Kendall test.

Figure 5. Lagged composites of normalized heating indices, which are heating anomalies averaged over (blue) the North Pacific (40-70°N/170°-140°W) and (red) the eastern Canada (40°-70°N/90°-60°W) domain, during SWI destructive events. Dots with thick lines indicate statistically significant values at 95% level computed by the Monte Carlo resampling method.

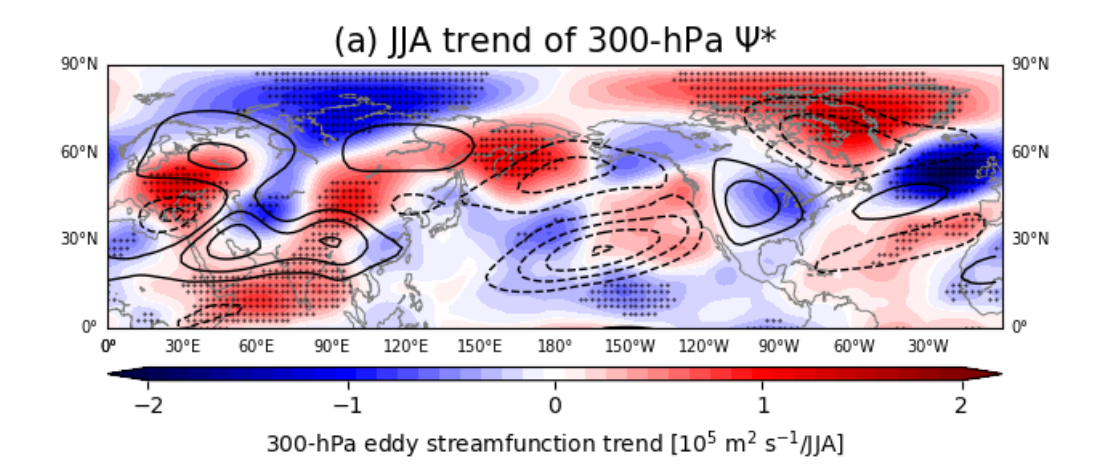
Figure 6. Pattern correlations from 360 patch experiments. At each grid point, the value represents uncentered pattern correlation between observed eddy streamfuction anomaly and model eddy streamfuntion response to the patch forcing centered at that grid point. Red shadings, or positive pattern correlations, indicate that the patch forcing centered at that location induces circulation that resembles the destructive interference pattern.

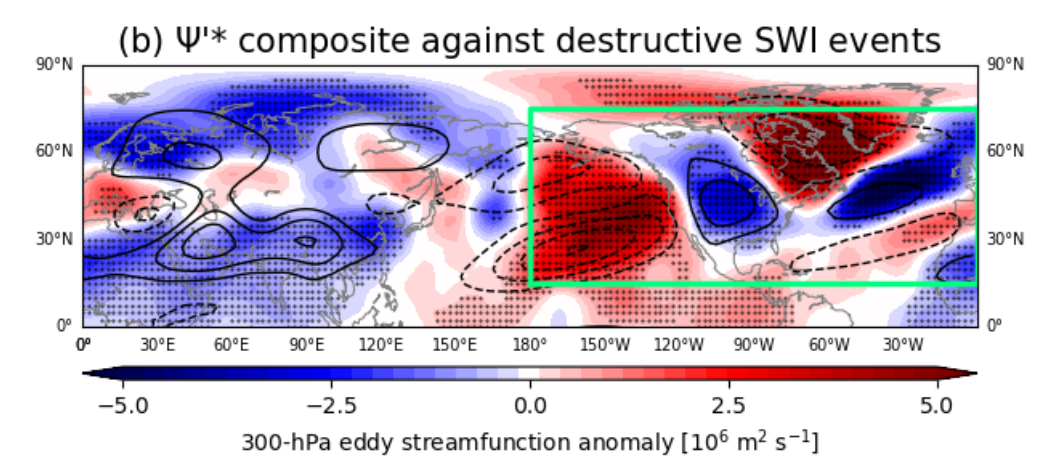
Figure 7. Area-averaged vertically integrated model tracer anomaly from 360 patch experiments. The value at each grid point represents (a) tracer anomaly averaged over 40°-70°N/90°-60°W domain (the red box) from model day 9 to 11, and (b) tracer anomaly averaged over 40-70°N/170°-140°W domain (the blue box) from model day 4 to 6, which results from

the patch forcing centered at that grid point (see section 4 for details). Red shadings, or positive tracer anomaly values, indicate that the patch forcing centered at the location increases tracer anomaly over the region in the box.

Figure 8. (a)-(d) The 300-hPa eddy streamfunction anomaly averaged over model days 6 to 16 (shading) in response to indicated patch forcings. The contours show observed 300-hPa eddy streamfunction anomaly composite, averaged from lag days -5 to +5 of SWI destructive events (contour interval is 6.0×10^5 m² s⁻¹; negative values are dashed and zero value is omitted). Pattern correlations between model streamfunction (shading) and observed composite (contours) are indicated. (e)-(h) Vertically integrated model tracer anomaly (shading) with vertically integrated model tracer flux anomaly (vectors) averaged over model day 9 to 11, in response to indicated patch forcings. Vectors with magnitude larger than 0.5 kg m⁻¹ s⁻¹ are plotted and the reference vector is 5 kg m⁻¹ s⁻¹. Red boxes of (e)-(h) indicates the eastern Canada domain (40°-70°N/90°-60°W).

Figure 9. Schematic diagrams of the heating-circulation relay mechanism during the evolution of the destructive interference pattern. The mechanism is illustrated in chronological order from (a) to (d). We refer readers to Conclusion section for details.





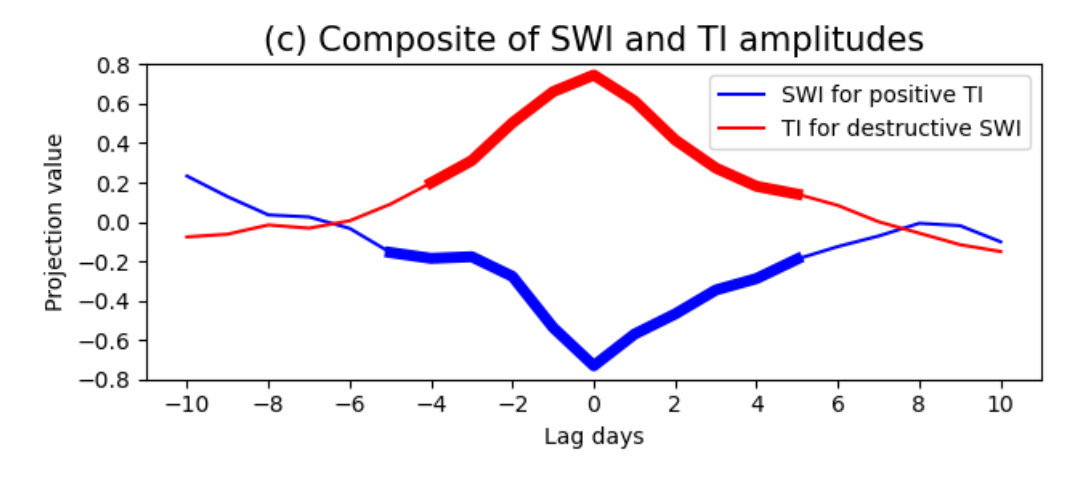


Figure 1. (a) The linear trend of June, July, and August 300-hPa eddy streamfunction during 1979-2017 (shading) and the 300-hPa climatological stationary wave (contour). Contour interval is 2.5×10^6 m² s⁻¹; negative values are dashed and zero value is omitted. (b) 300-hPa eddy streamfunction anomaly composite for destructive stationary wave interference (SWI) index at lag day 0 (shading). The contours are as in (a). Green box indicates the projection domain of SWI (c) Lagged composite of SWI against positive events of trend index (TI; blue line), and lagged composite of TI against SWI destructive events (red line). Dotted areas in (a) indicate statistical significance at the 95% level as computed by the Mann-Kendall test, and dotted areas in (b) and thick line in (c) indicate statistically significant values at the 95% level as computed by Monte Carlo resampling method.

Composites of streamfuntion and T2M during SWI destructive events

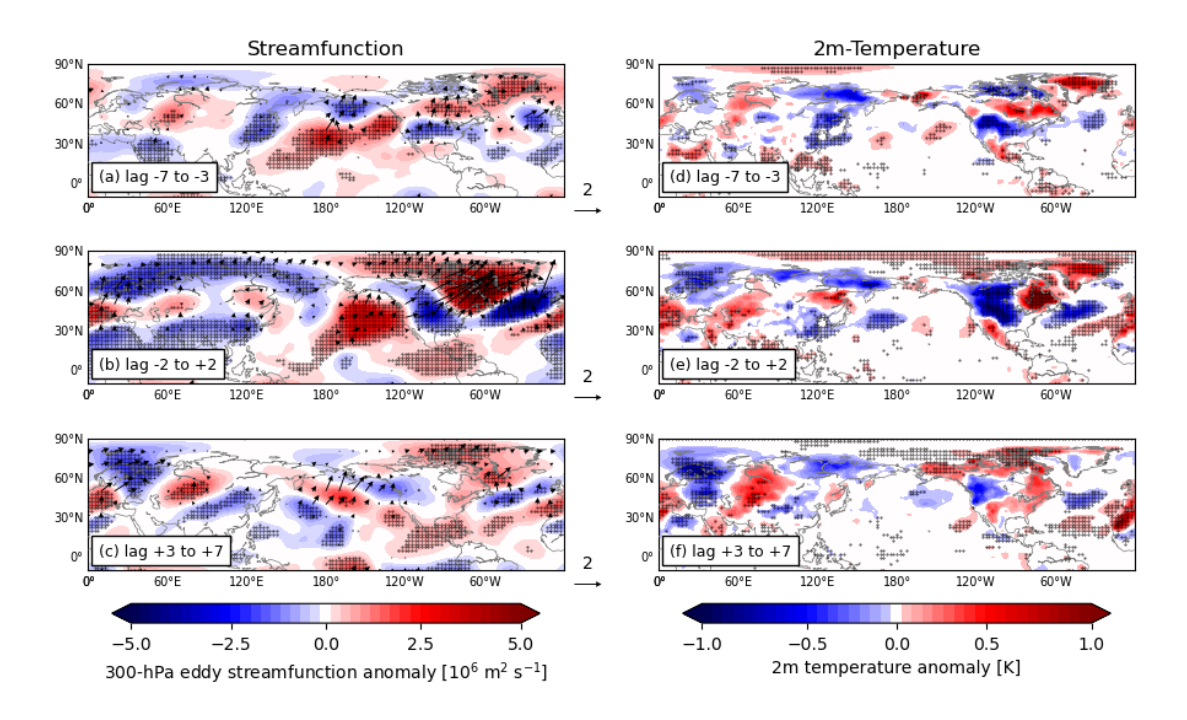


Figure 2. Pentad composites of (a)-(c) 300-hPa eddy streamfunction anomaly (shading) with wave activity flux (vectors) and (d)-(f) 2m-temperature anomaly. Vectors with magnitude larger than 0.1 m² s⁻² are plotted and the reference vector is 2 m² s⁻². Pentads are centered at lag days –5, 0, and +5 of destructive stationary wave interference (SWI) events. Dotted areas represent statistical significance at the 95% level as computed by the Monte Carlo resampling method.

Composites of latent heating and moisture flux convergence during SWI destructive events

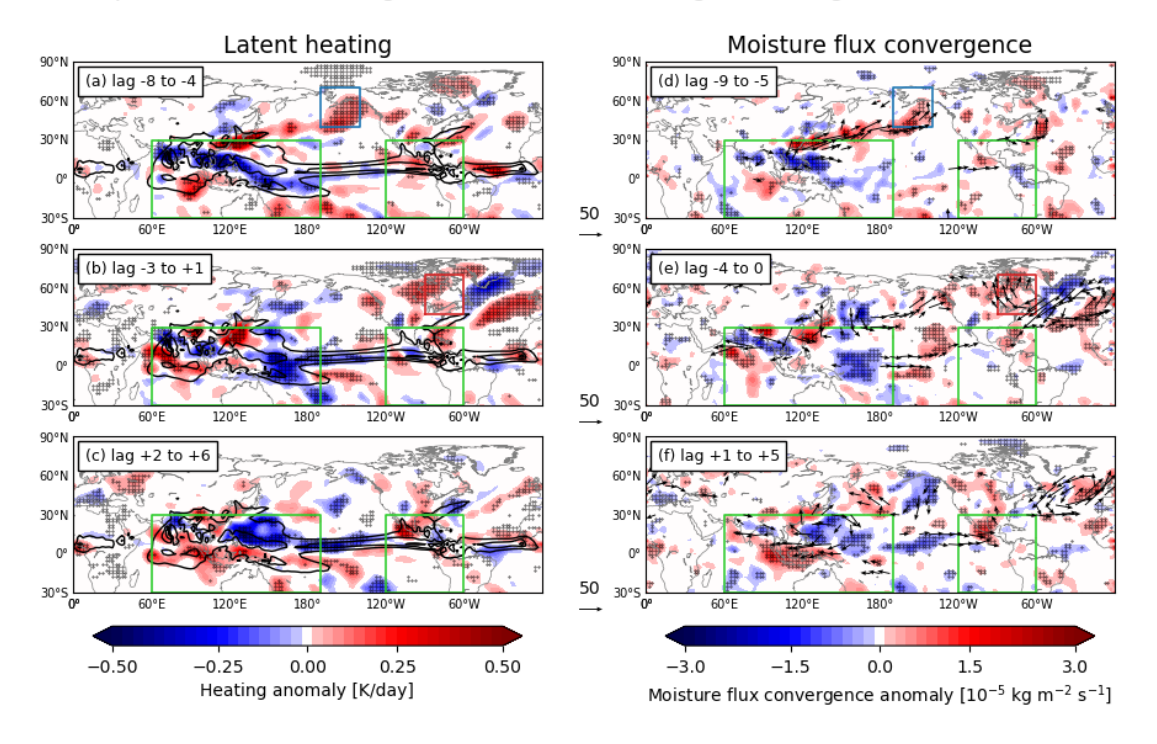


Figure 3. (a)-(c) Pentad composites of latent diabatic heating anomaly (shading) and June, July, and August (JJA) climatological heating (contour; 2, 4, and 6 K/day values are plotted). (d)-(f) Pentad composites of vertically integrated water vapor flux anomaly (vectors) with vertically integrated moisture flux convergence anomaly (shading). Vectors with magnitude larger than 20 kg m⁻¹ s⁻¹ are plotted and the reference vector is 50 kg m⁻¹ s⁻¹. Pentads are centered at lag days (a)-(c) –6, -1, and +4, and (d)-(f) -7, -2, and +3 of destructive stationary wave interference (SWI) events. Dotted areas represent statistical significance at the 95% level as computed by the Monte Carlo resampling method. Green boxes represent two domains of tropical heating projection index (HPI) and blue and red boxes represent the North Pacific domain and the eastern Canada domain (see section 3 for details).

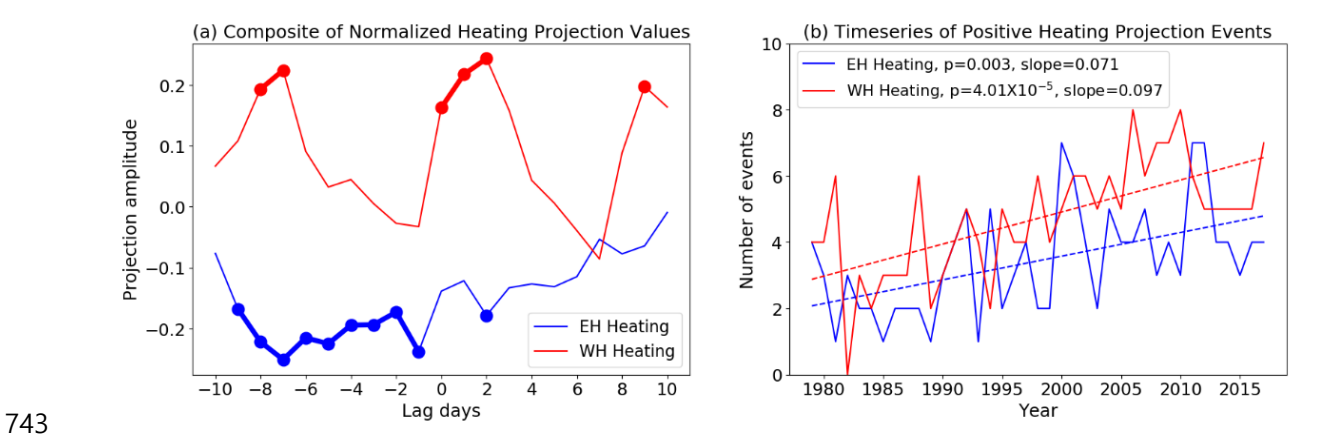


Figure 4. (a) Lagged composite of normalized heating projection amplitudes of (blue) the EH-heating and (red) the WH-heating during destructive stationary wave interference (SWI) events. Dots with thick lines indicate statistically significant values at the 95% level as computed by the Monte Carlo resampling method. (b) Timeseries of the number of positive heating projection events per each year. The blue and the red line indicate the heating projection over EH-heating domain and the WH-heating domain, respectively. Dashed lines indicate linear fit lines of each timeseries. Indicated p-values are computed by the Mann-Kendall test.

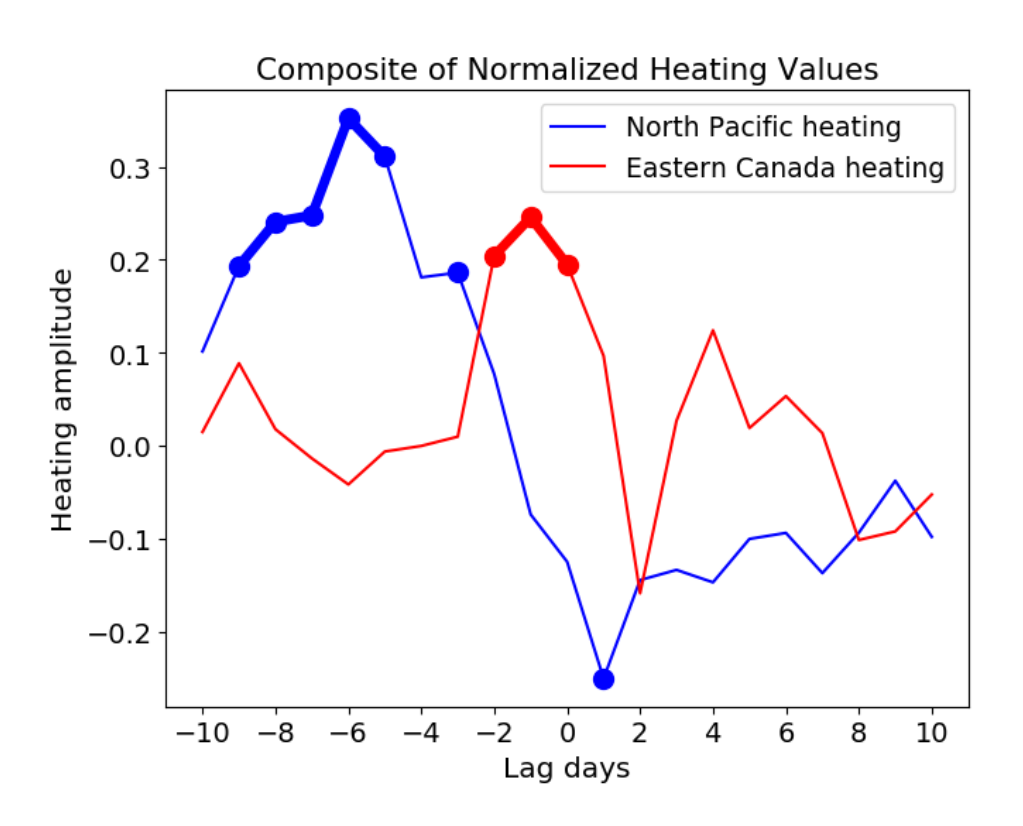


Figure 5. Lagged composites of normalized heating indices, which are heating anomalies averaged over (blue) the North Pacific (40-70°N/170°-140°W) and (red) the eastern Canada (40°-70°N/90°-60°W) domain, during SWI destructive events. Dots with thick lines indicate statistically significant values at 95% level computed by the Monte Carlo resampling method.

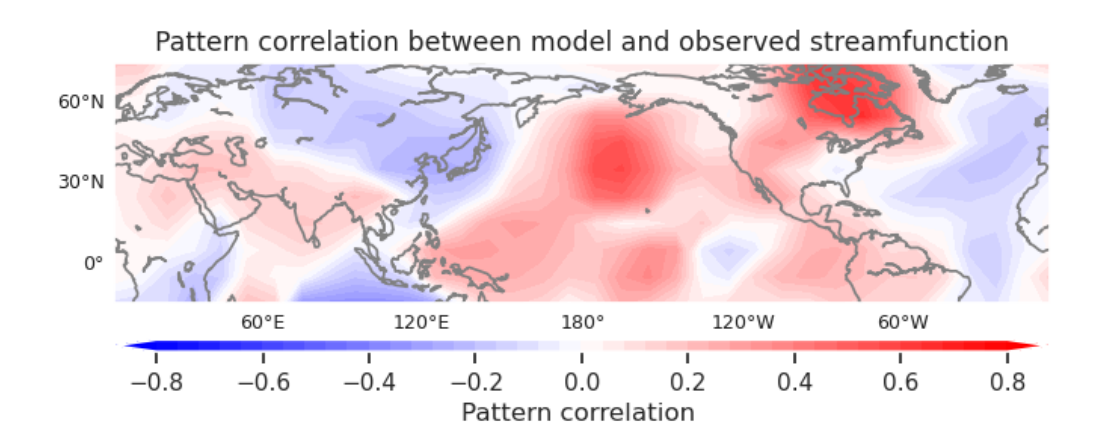
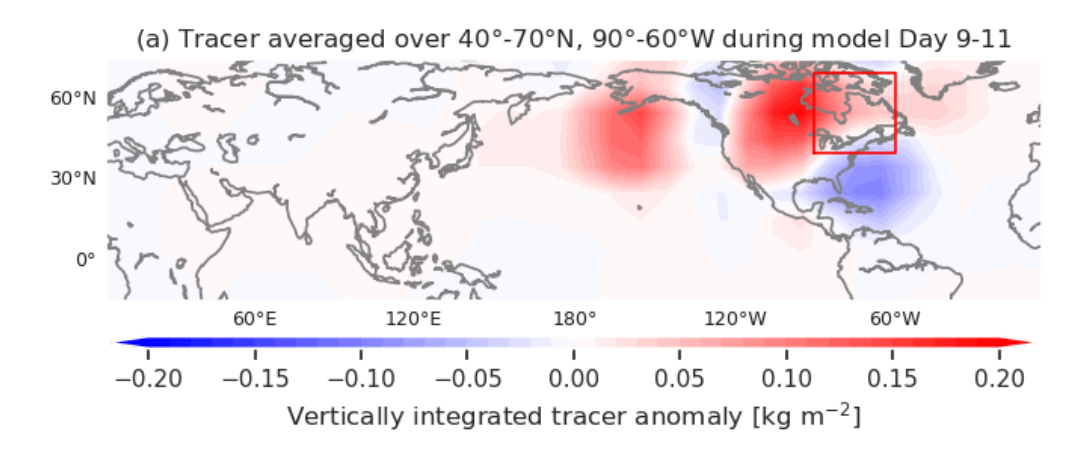


Figure 6. Pattern correlations from 360 patch experiments. At each grid point, the value represents uncentered pattern correlation between observed eddy streamfuction anomaly and model eddy streamfuntion response to the patch forcing centered at that grid point. Red shadings, or positive pattern correlations, indicate that the patch forcing centered at that location induces circulation that resembles the destructive interference pattern.



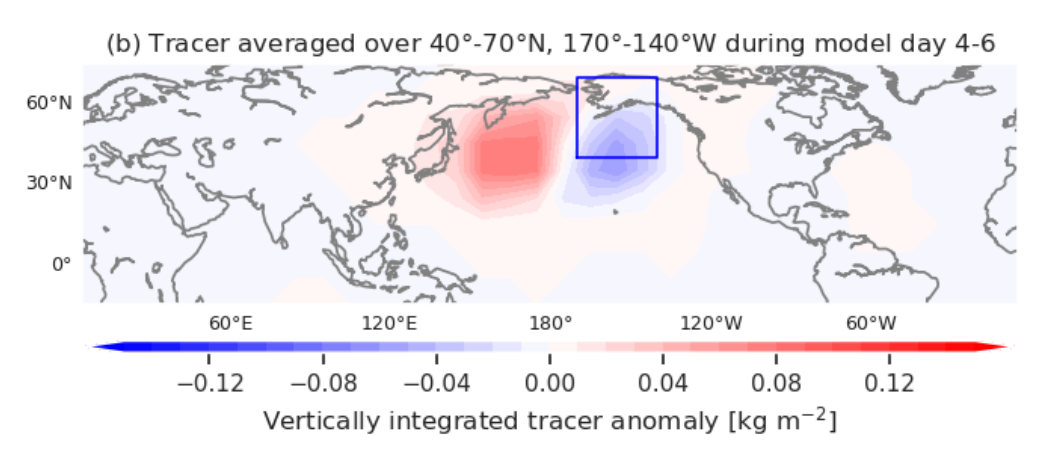


Figure 7. Area-averaged vertically integrated model tracer anomaly from 360 patch experiments. The value at each grid point represents (a) tracer anomaly averaged over 40°-70°N/90°-60°W domain (the red box) from model day 9 to 11, and (b) tracer anomaly averaged over 40-70°N/170°-140°W domain (the blue box) from model day 4 to 6, which results from the patch forcing centered at that grid point (see section 4 for details). Red shadings, or positive tracer anomaly values, indicate that the patch forcing centered at the location increases tracer anomaly over the region in the box.

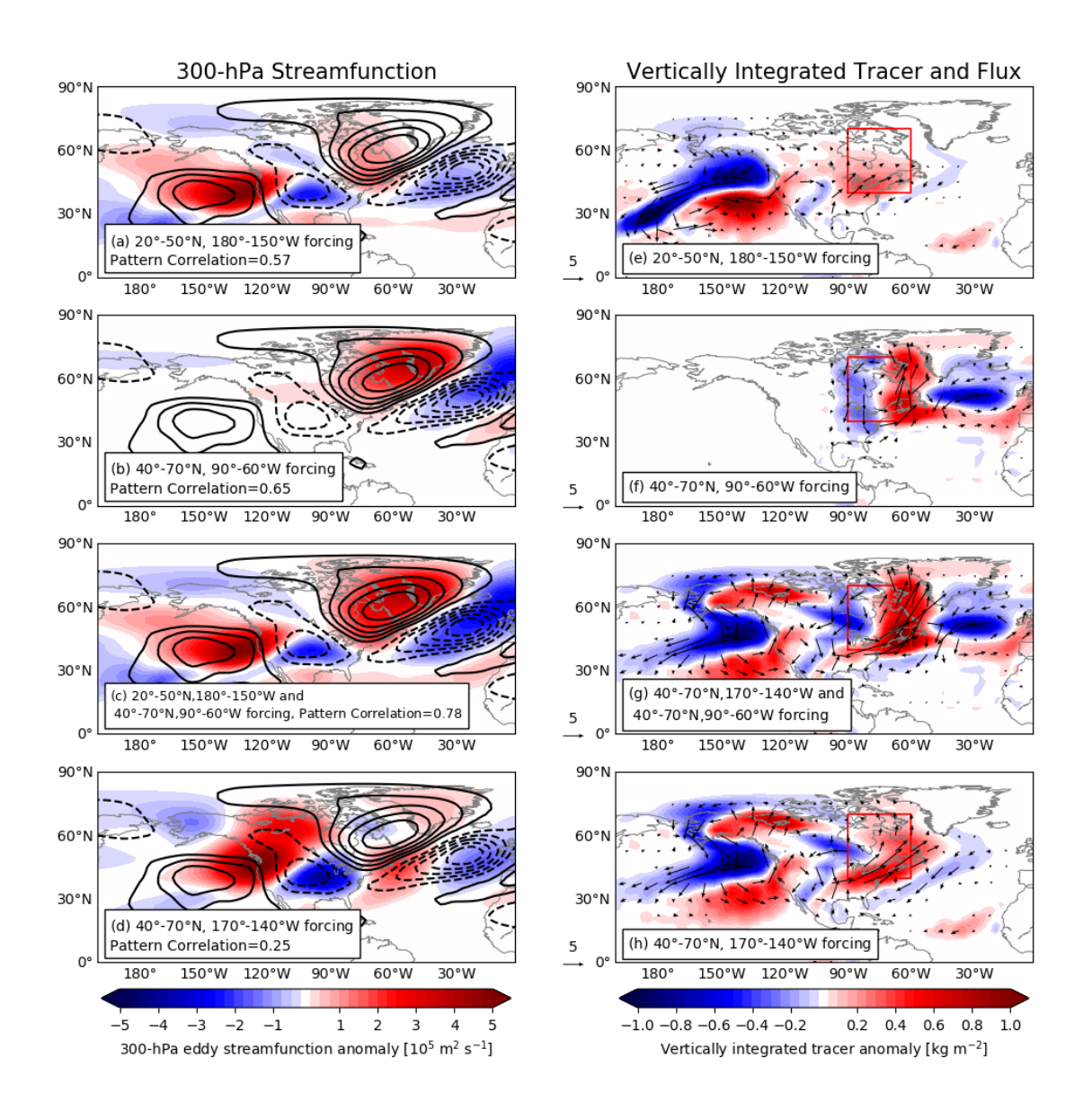


Figure 8. (a)-(d) The 300-hPa eddy streamfunction anomaly averaged over model days 6 to 16 (shading) in response to indicated patch forcings. The contours show observed 300-hPa eddy streamfunction anomaly composite, averaged from lag days -5 to +5 of SWI destructive events (contour interval is 6.0×10^5 m² s⁻¹; negative values are dashed and zero value is omitted). Pattern correlations between model streamfunction (shading) and observed composite (contours) are indicated. (e)-(h) Vertically integrated model tracer anomaly (shading) with vertically integrated model tracer flux anomaly (vectors) averaged over model day 9 to 11, in response to indicated patch forcings. Vectors with magnitude larger than 0.5 kg m⁻¹ s⁻¹ are plotted and the reference vector is 5 kg m⁻¹ s⁻¹. Red boxes of (e)-(h) indicates the eastern Canada domain (40°-70°N/90°-60°W).

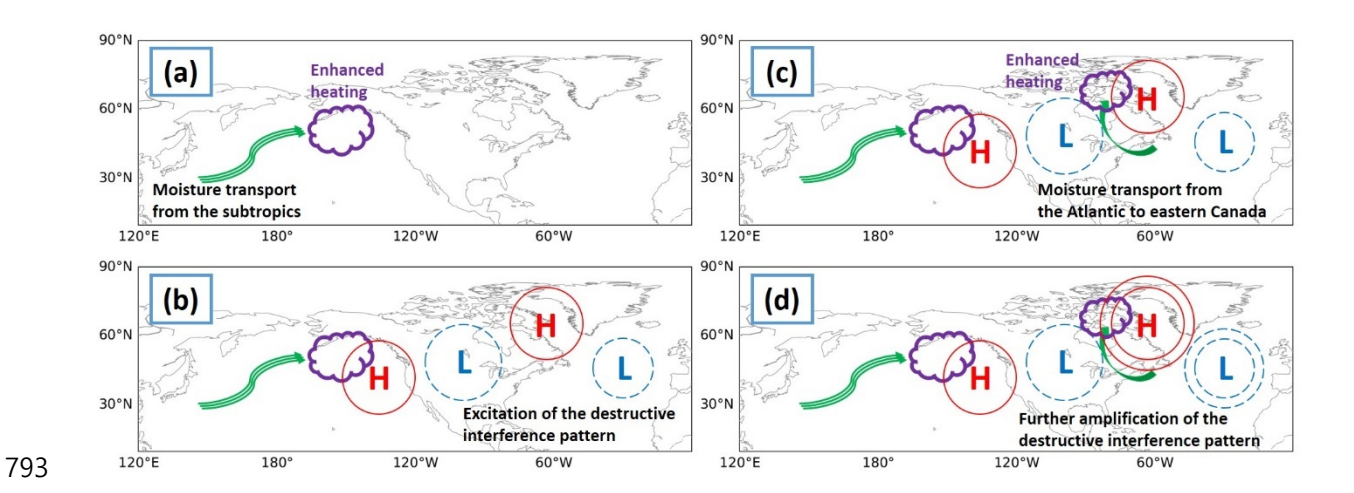


Figure 9. Schematic diagrams of the heating-circulation relay mechanism during the evolution of the destructive interference pattern. The mechanism is illustrated in chronological order from (a) to (d). We refer readers to conclusion section for details.